Supplementary Note 1: Preparation and Characterization of thermally expanded h-BN

EXPERIMENTAL SECTION

Preparation of Thermally Expanded BN: This step involves a thermal expansion of the commercial h-BN powder (from Aldrich, ~1 μm, 98% purity) using a tubular oven. 100 mg of commercial h-BN powder was placed into a quartz basket inside the oven and heated up to 1000 ºC for 10 min.

Shear Mixing of the thermally expanded h-BN powder: 10 mg of the thermally expanded h-BN powder was put into a 20 mL vial with 10 mL of a (4:1) 2-Propanol/H_2O (v/v) mixture. The sample was then dispersed with a shear-mixer device (IKA Ultra Turrax T25 digital) for 90 min at 25000 rpm. In the next step, the resulting suspension was centrifuged for 10 min at 4000 rpm in order to homogenize the sample.

Characterization: Atomic Force Microscopy (AFM) from Nanotec Electronica SL. WSxM software (www.wsxm.es) was employed both for data acquisition and image processing [R1,R2]. The AFM topographical images were acquired in contact mode to avoid possible artefacts in the flake thickness measurements [R3]. OMCL-RC800PSA cantilevers (www.probe.olympus-global.com) with a nominal spring constant of 0.05 N/m and tip radius of 15 nm were employed. Low forces of the order of 100 pN were used for imaging to ensure that the flakes would not be deformed by the tip. For the AFM measurements, 15 μL of the expanded h-BN suspension were casted on a SiO_2 surface and dried after 15 min. under an Ar flow. Scanning Electron Microscopy (SEM) imaging was performed on a Philips XL 30 S-FEG microscope operating at an accelerating voltage of 10 kV. The Infrared (IR) measurements were carried out using a SHIMADZU FTIR 8400S with a maximum resolution of 0.85 cm^{-1}. X-ray Power Diffraction (XRPD) patterns were measured on a Bruker D8 Advance with Cu Kα radiation with rapid detector (lynxeye). Transmission Electron Microscopy (TEM) images were obtained in a JEOL JEM 3000F TEM system with an accelerating voltage of 300 kV. For the TEM measurements, 15 μL of the suspension was casted on a TEM grid and left to dry. X-ray Photoelectron Spectroscopy (XPS) measurements were performed on SiO_2 substrate using a Thermo Scientific K-Alpha spectrometer.

RESULTS AND DISCUSSION

Thermal expansion of h-BN is a suitable method to produce few layer h-BN. Supplementary Figure 1(a) shows the Fourier-Transform Infrared Spectroscopy (FTIR) analysis of the expanded h-BN powder, where the two characteristic peaks of pristine h-BN at 1340 and 803 cm^{-1} (representing the in-plane B–N stretching and out-of-plane B–N bending vibration, respectively) are present. A weaker band at ~3200 cm^{-1}, corresponding to O–H vibrations of adsorbed water molecules and typically observed in pristine h-BN, is also present.

The XRPD difractogram of expanded h-BN in Supplementary Figure 1(b) shows peaks at 2θ = 26.8°, 41.7° and 55.2°, which correspond to the (002), (100), and (004) planes, respectively, of pristine h-BN.

Finally, the chemical composition analysis of the expanded h-BN carried out by the XPS (Supplementary Figures 1(c) and 1(d)) confirm that this new material consists of

only boron and nitrogen atoms. The N1s XPS spectrum of the expanded h-BN shows in Supplementary Figure 1(c) a band at 397.9 eV assigned to N–B bond. The B1s band displayed in Supplementary Figure 1(d) is fitted using only the component of the B–N bond (190.4eV).

In summary, the sample characterization techniques employed in this work confirm that the expanded h-BN corresponds to an h-BN structure in which neither structural nor compositional changes, such as oxygen incorporation during the thermal expansion process, can be detected.

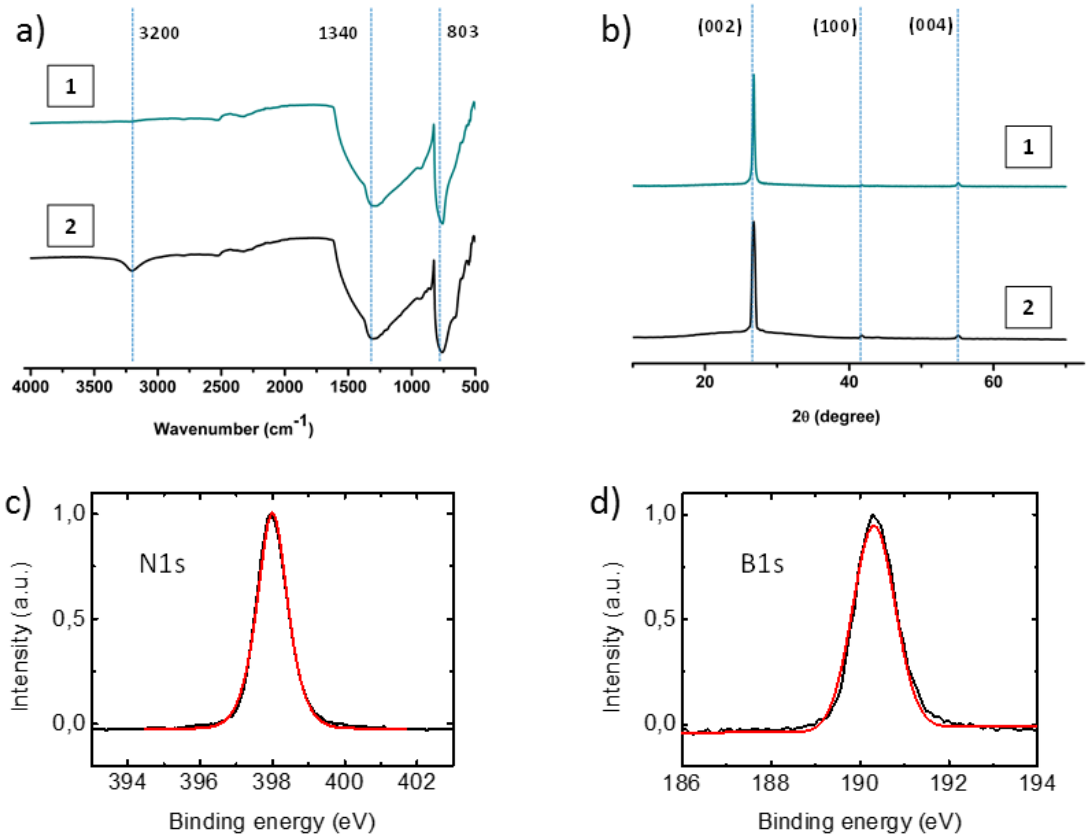

Supplementary Figure 1. (a) Fourier-transform infrared spectroscopy traces of pristine h-BN (1) and thermally expanded h-BN (2), (b) X-ray power diffraction of pristine h-BN (1) and expanded h-BN (2). X-ray photoelectron spectroscopy spectra of the expanded h-BN showing N1s band (c) and the B1s band (d).

To study the morphology of the thermally expanded h-BN powder, we performed the SEM analysis in Supplementary Figure 2. Supplementary Figures 2(a) and 2(b) show pristine h-BN with dimensions of few hundreds of nanometers and smooth surfaces and edges. Supplementary Figures 2(c) and 2(d) show a typical morphology of the thermally expanded h-BN powder, which consists of plate aggregates of h-BN particles with rough edges.

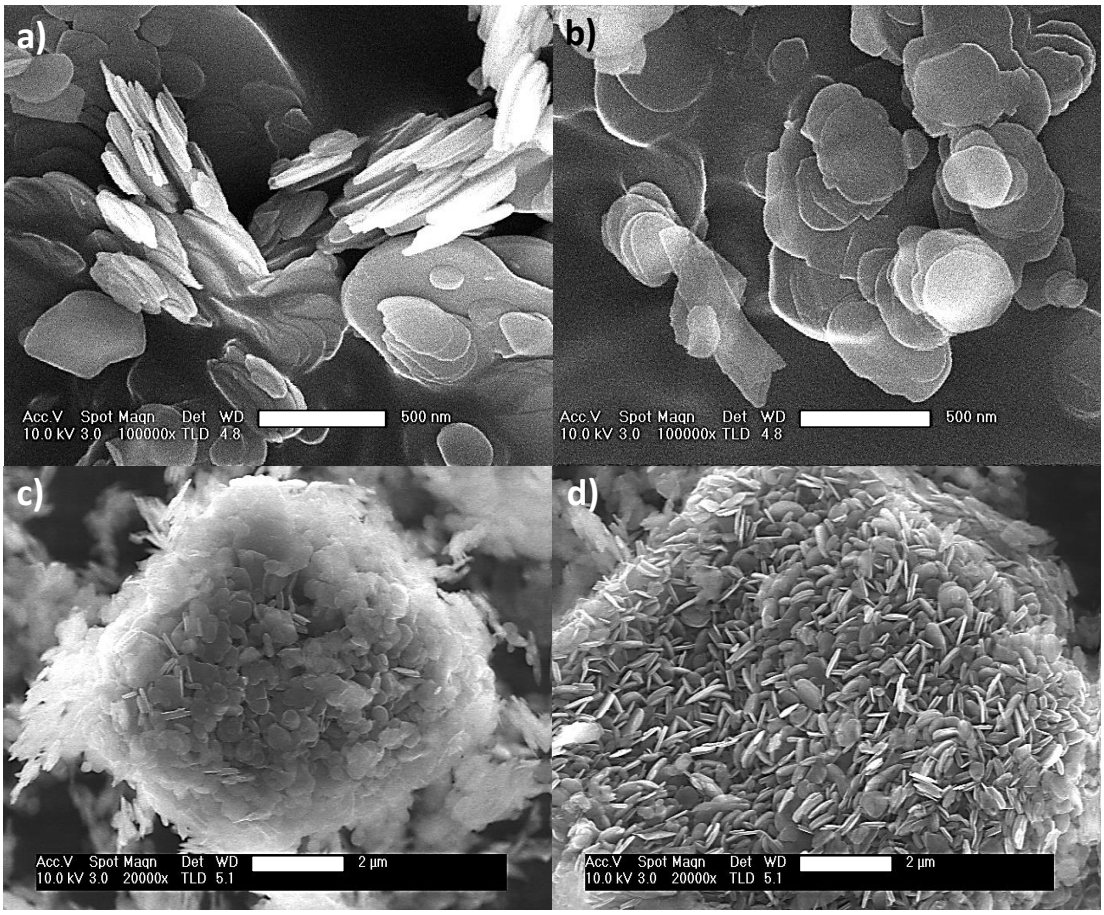

Supplementary Figure 2. Scanning electron microscopy images recorded at two different magnifications of (a), (b) commercial h-BN powder from "Aldrich Co." (~1 µm, 98% purity) and (c), (d) h-BN powder after thermal expansion.

AFM analysis of the expanded h-BN sample displayed in Supplementary Figure 3(a) shows a thickness of *ca*. 3.5-4.5 nm and lateral dimensions of *ca*. 300×200 nm. These lateral dimensions correlated well with those observed by TEM in Supplementary Figure 3(b).

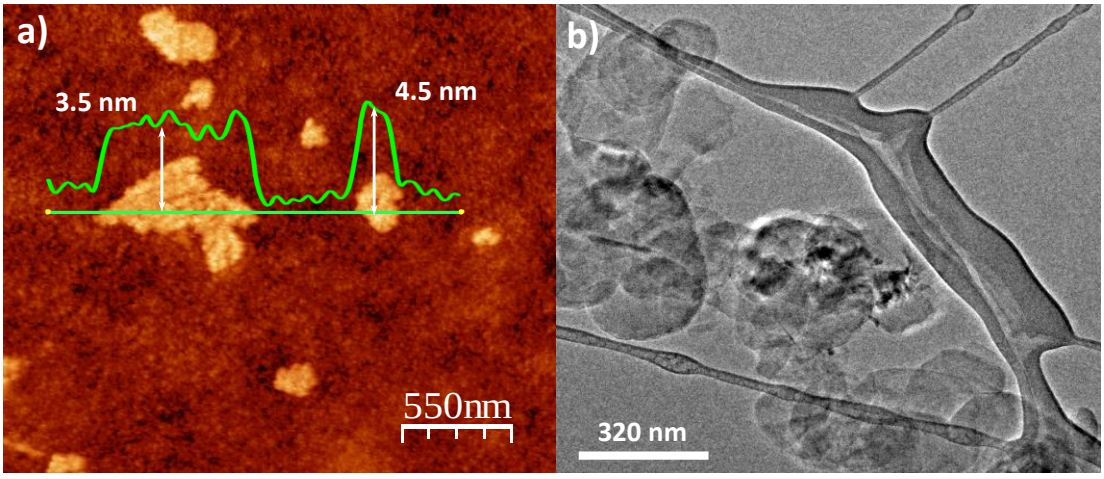

Supplementary Figure 3. (a) Atomic force microscopy and (b) Transmission electron microscopy image of the thermally expanded h-BN.

Supplementary Note 2: Wide span of defect-state emission wavelengths in h-BN

The low-temperature micro-PL spectrum in Supplementary Figure 4, recorded using 442 nm continuous-wave (cw) laser excitation in the absence of the SAW, reveals multiple sharp PL peaks with linewidths below 1.5 meV. For each position of the focused laser spot on the sample, we observe a unique pattern of the emission lines covering a broad spectral range between ~450 to 700 nm. Some of these lines are observed up to room temperature with rather standard temperature-induced linewidth broadening and PL quenching. They also exhibit asymmetric line-shapes with pronounced low-energy tails, which are maintained at low temperatures, typically found in h-BN and attributed to interactions with phonons [R4,R5].

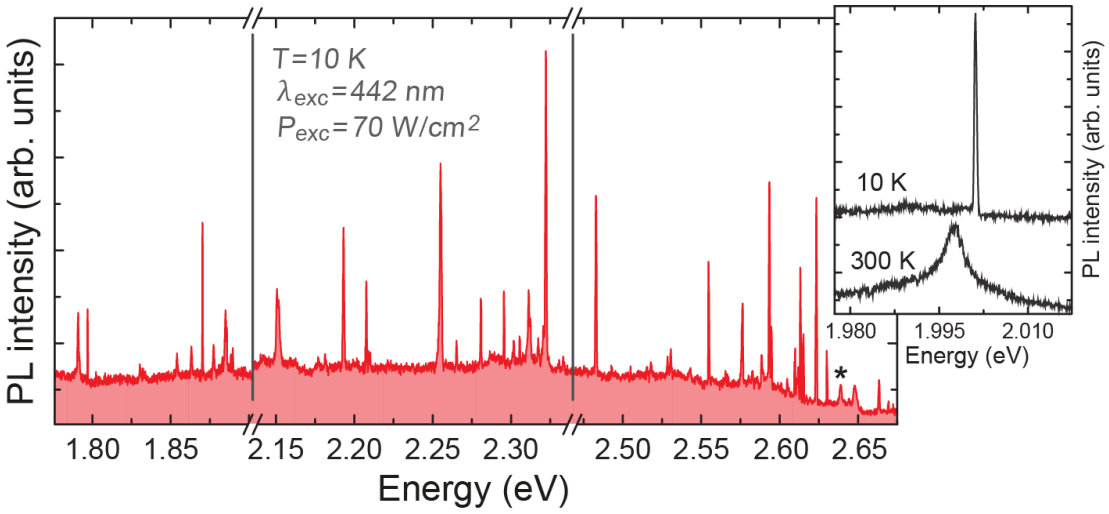

Supplementary Figure 4. Representative micro-PL spectrum excited at 442 nm and recorded for the excitation power density of 70 W/cm^2 at 10 K showing a broad forest of narrow emission lines spanning across a wide energy range of ~900 meV. The inset shows temperature-broadened emission lines with asymmetric low-energy tail. The asterisk denotes the E_{2g} Raman mode of h-BN.

Supplementary Note 3: Normalization and deconvolution method in the photon correlation study

To obtain the intensity correlation function $g^{(2)}(\tau)$, the measured delay time histogram is normalized to that of a Poissonian source in the following way [R6,R7]: the raw coincidence rate counted during the total integration time T_{int} within a time bin of width t_{bin} is divided by $r_1 \cdot r_2 \cdot t_{\mathrm{bin}} \cdot T_{\mathrm{int}}$, where r_1 and r_2 are the count rates on each detector. The deviation from an ideal zero-antibunching value in our experiments could be explained by the random coincidences caused by uncorrelated background PL from the host grains, as well as the limited temporal resolution of our detection setup and the presence of bunching caused by long-living metastable states [R8]. Because of the high value of the signal-to-background ratio (which was independently estimated from the PL spectrum recorded for each photon correlation histogram), the background correction was not performed since its contribution to the antibunching is negligible

[R6,R7]. Thus, the residual counts at zero time delay mainly result from the photon bunching and the instrument response function (IRF) of our detection system.

To quantify the single-photon performance, we fit our experimental results with the expected three-level second-order auto-correlation function $g^{(2)}_{\text{ideal}}(\tau) = 1 - A_1 \cdot e^{-|\tau/\tau_1|} + A_2 \cdot e^{-|\tau/\tau_2|}$, convolved with the IRF (which is mainly determined by the time jitter of the single-photon detectors) of the form of $h(\tau) = C \cdot e^{-|\tau/\tau_{\text{IRF}}|}$. The resulting fitting function is as follows:

$$g^{(2)}_{\text{meas}}(\tau) = \int_{-\infty}^{\infty} h\left(\tau - \tau'\right) g^{(2)}_{\text{ideal}}\left(\tau'\right) d\tau'$$

$$= 1 - A_1 \cdot \frac{\tau_1^2 \cdot \tau_{\text{IRF}}}{\tau_{\text{IRF}}^2 - \tau_1^2}\left(\frac{e^{-\left|\frac{\tau}{\tau_{\text{IRF}}}\right|}}{\tau_1} - \frac{e^{-\left|\frac{\tau}{\tau_1}\right|}}{\tau_{\text{IRF}}}\right) + A_2 \cdot \frac{\tau_2^2 \cdot \tau_{\text{IRF}}}{\tau_{\text{IRF}}^2 - \tau_2^2}\left(\frac{e^{-\left|\frac{\tau}{\tau_{\text{IRF}}}\right|}}{\tau_2} - \frac{e^{-\left|\frac{\tau}{\tau_2}\right|}}{\tau_{\text{IRF}}}\right), \quad (1)$$

In the above expressions, τ is the time delay between photons detected at the two HBT detectors, A_1 and τ_1 are the antibunching dip and time constant, A_2 and τ_2 are the bunching amplitude and time constant, respectively, C is the normalization factor and τ_{IRF} ~350 ps is the temporal resolution of the HBT detectors.

At zero time delay ($\tau = 0$), the measured photon correlation is thus determined by:

$$g^{(2)}_{\text{meas}}(0) = 1 - A_1 \cdot \frac{\tau_1}{\tau_1 + \tau_{\text{IRF}}} + A_2 \cdot \frac{\tau_2}{\tau_2 + \tau_{\text{IRF}}}. \quad (2)$$

The quality of a single-photon emitter is then given by the antibunching value:

$$g^{(2)}(0) = 1 - A_1 + A_2, \quad (3)$$

where A_1 and A_2 are extracted from fitting Supplementary Equation (1) to the measured data.

Supplementary Note 4: Single-photon emission at cryogenic and room-temperature

Supplementary Figure 5 shows second-order auto-correlation functions measured at low- and room-temperature for single, spectrally filtered PL lines from the same defect centre (different from those corresponding to ZPL_1, ZPL_2 and ZPL_3 emission lines discussed in the main paper), excited using cw optical excitation. The photon antibunching is maintained up to room-temperature. The resulting $g^{(2)}(0)$ values are indicated in Supplementary Figures 5(b) and 5(e).

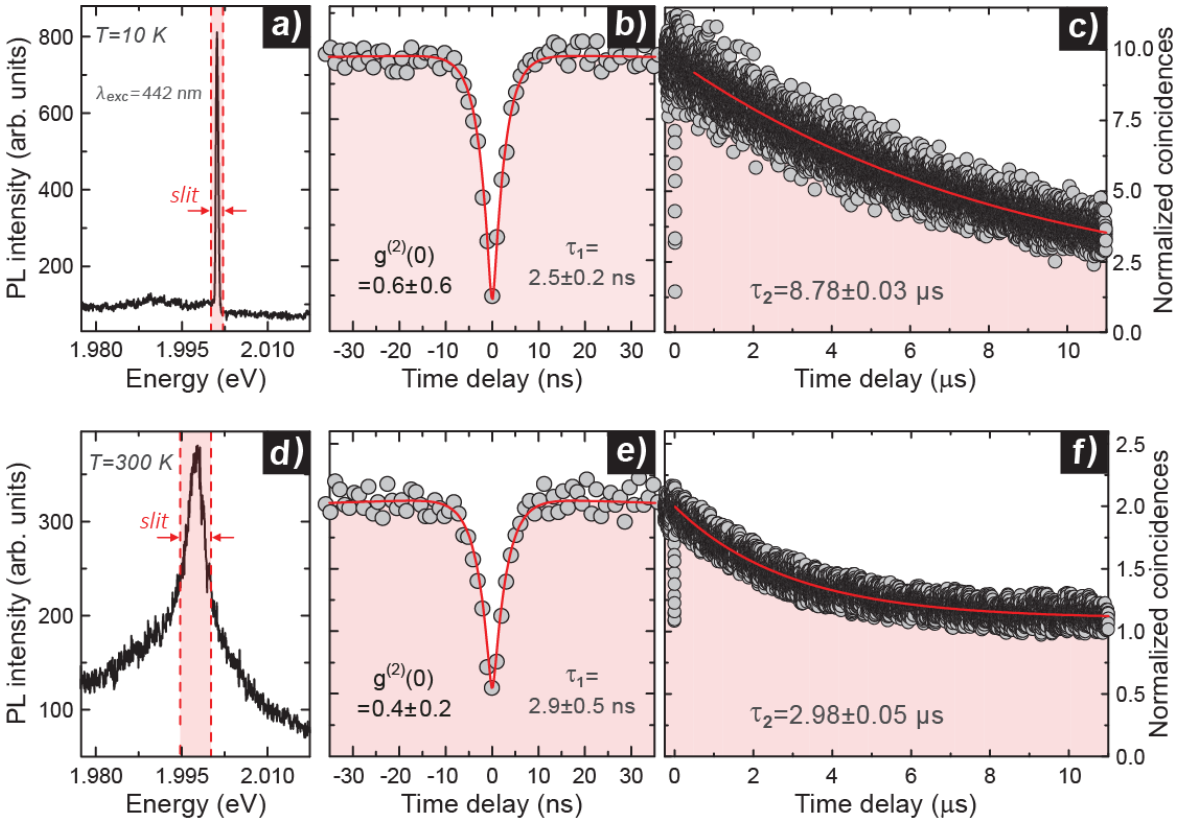

Supplementary Figure 5. (a),(d) Emission spectrum of a single h-BN defect excited with a 442 nm continuous-wave laser and recorded for the excitation power density of 70 W/cm^2 at 10 K (a) and 300 K (d). The dashed vertical lines represent the spectral window sent to the HBT interferometer. (b),(c),(e),(f) Normalized second-order auto-correlation function measured under the same excitation conditions as the corresponding. PL spectra. The short timescale (tens of nanoseconds) in (b) and (e) shows antibunching, while the long timescale (tens of microseconds) in (c) and (f) reveals the presence of photon bunching.

Supplementary Note 5: Numerical calculation of the SAW-induced strain and piezoelectric fields

The strain and piezoelectric fields of the SAW propagating on the surface of a 128° Y-cut $LiNbO_3$ substrate are calculated in Supplementary Figure 6 by solving the coupled elastic and electromagnetic equations according to the numerical model described in Ref. [R9]. The $x-$, $y-$ and $z-$components are referenced to the $LiNbO_3$ crystal axes designated in Fig. 1 of the main paper. The calculations take into account the acoustic power conversion efficiency discussed in the Methods section of the main paper.

The dependence of the axial strain components (ε_{XX}, ε_{YY} and ε_{ZZ}) and of the hydrostatic strain ($s_0 = \varepsilon_{XX} + \varepsilon_{YY} + \varepsilon_{ZZ}$) on the acoustic amplitude is estimated in Supplementary Figure 6(a) at fixed acoustic phase corresponding to the maximum tensile strain along the SAW propagation direction (i.e. x-axis in Fig. 1). As shown in Supplementary Figure 6(b), at these acoustic phases, only the transverse component (i.e. f_z parallel to the z-axis in Fig. 1) of the SAW-induced oscillating piezoelectric field is present. On the contrary, as seen in Supplementary Figures 6(c) and 6(d), at the

SAW phase at which the strain vanishes only the longitudinal piezoelectric field component (f_x) parallel to the SAW propagation direction (i.e. x-axis) is present.

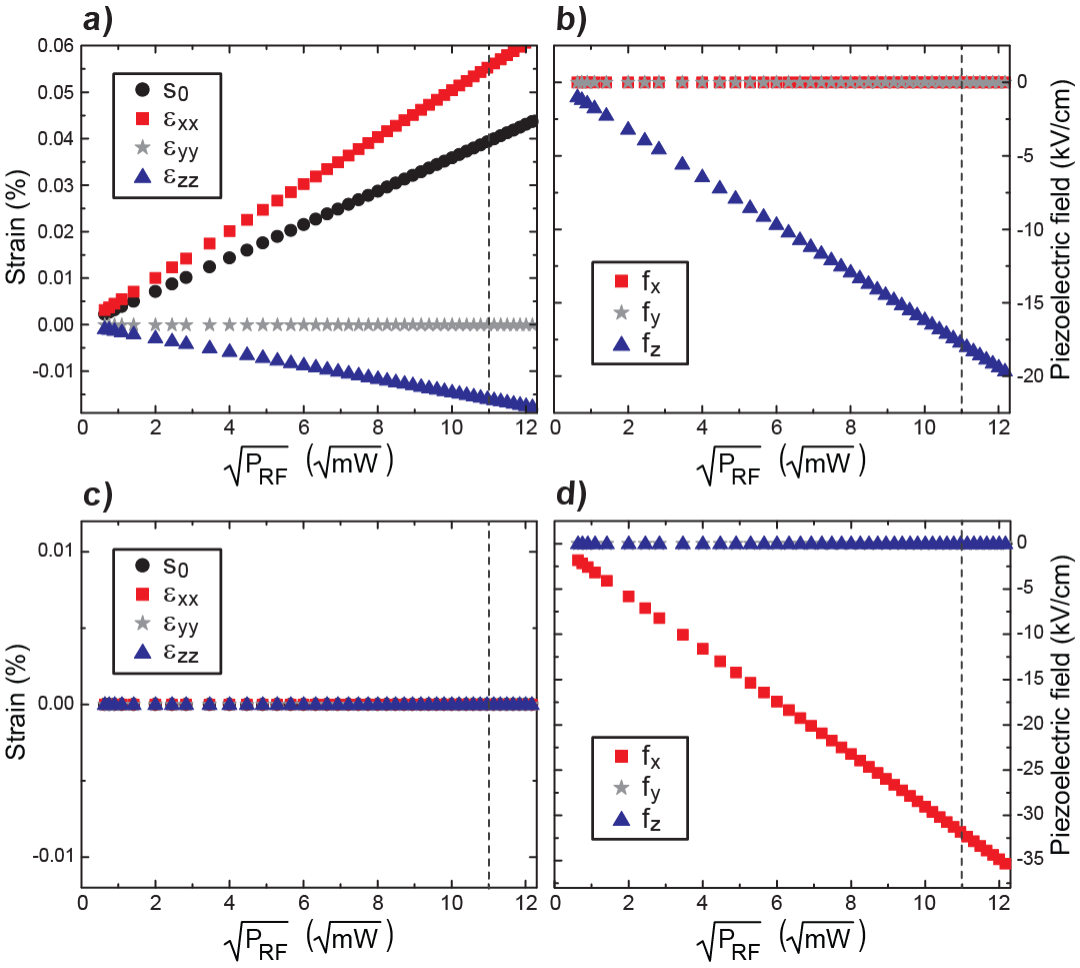

Supplementary Figure 6. Calculated (a),(c) strain (ε_{XX}, ε_{YY} and ε_{ZZ}) and (b),(d) piezoelectric field (f_X, f_Y and f_Z) components induced by the SAW propagating on the surface of $LiNbO_3$ for a range of SAW amplitudes used in our experiments. Red squares denote the $x-$, grey stars the $y-$ and blue triangles the $z-$direction. The resulting hydrostatic strain s_0 is represented by black circles in (a) and (c). The fields are calculated at the SAW phase corresponding to: (a),(b) maximum ε_{XX} and (c),(d) vanishing strain value. The vertical dashed line designates the acoustic amplitude for the highest radio-frequency power applied to the acoustic transducer.

Supplementary Note 6: Relation between the optical polarization degree and orientation and the acoustically governed fine-spectral tuning

Supplementary Figures 7(a) and 7(b) show the linear polarization degree (DOLP in the upper panels), direction of the polarization axis with respect to the SAW propagation vector (θ in the middle panels) and the magnitude of the SAW-induced splitting (ΔE in the lower panels) of the ZPL emission for a number of optically probed h-BN defects (all emitting at different energies) subjected to the propagating acoustic wave. For a randomly oriented emitter, the measured degree of polarization and the direction of the long axis depend on the actual (3D) orientation of its transition dipole relative to the optical axis of the collection optics. Thus, the conventional polarization-resolved far-

field microscopy, in general, provides information only about the orientation of the projection of the transition dipole moment onto the focal plane. The polarization angles θ depicted in Supplementary Figure 7, therefore, represent the in-plane orientation (i.e. within the sample plane in Fig. 1) of the emitting dipoles.

Our experimental data in Supplementary Figure 7(c) does not reveal any obvious correlation between neither the degree of linear polarization nor the in-plane polarization angle and the magnitude of the SAW-mediated spectral modulation. Instead, the dipoles, both showing the SAW-induced line spitting as well as those without such effect, appear to be nearly uniformly distributed at random (in-plane) angles and with random degree of polarization. Such behavior is already evident in Fig. 2 of the main paper, where ZPL1, ZPL2 and ZPL2 exhibit random well-defined in-plane projections of the emission dipoles that are clearly not aligned with the SAW propagating direction.

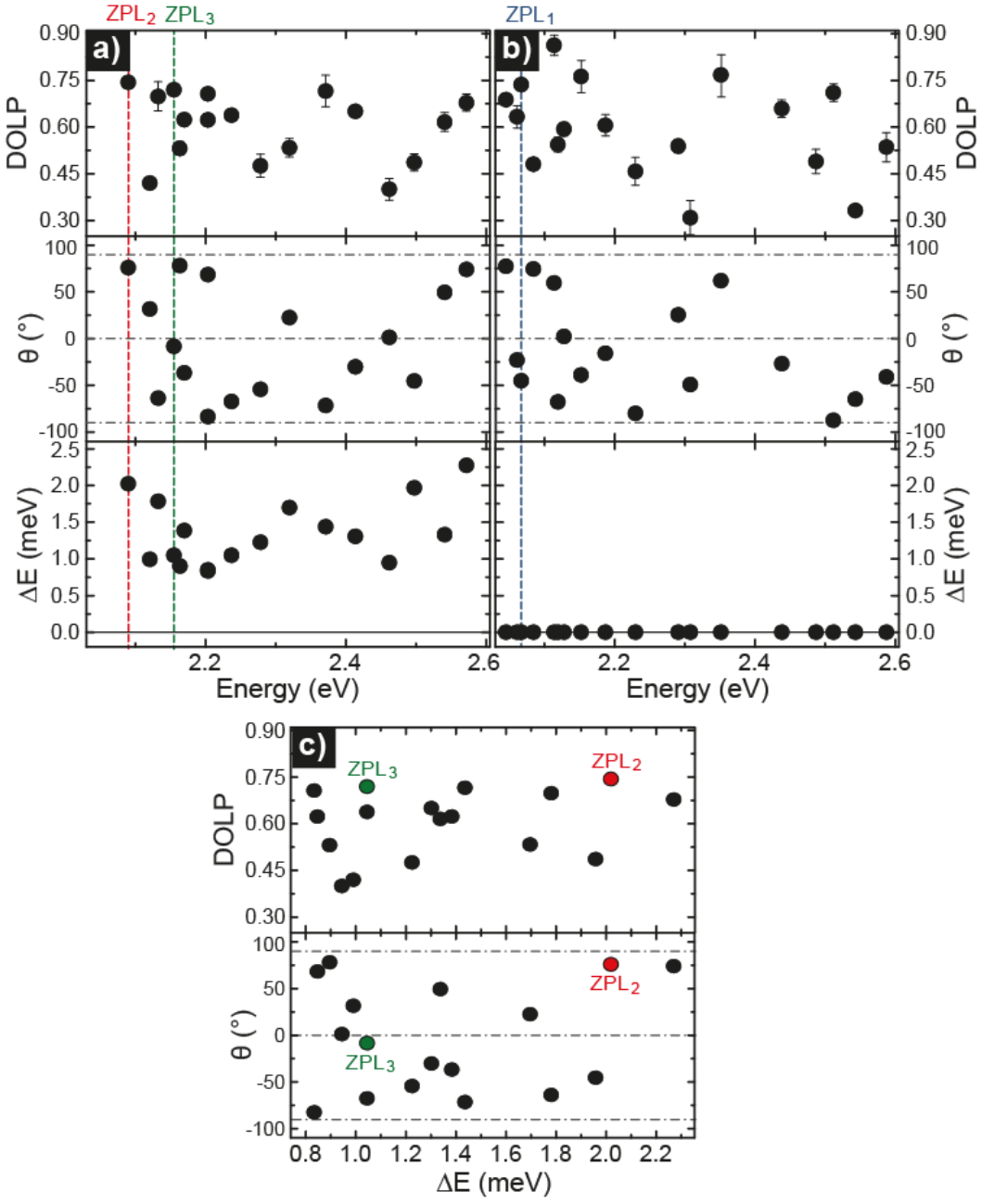

Supplementary Figure 7. SAW-induced splitting of the ZPL emission (ΔE, lower panels), in-plane polarization angle with respect to the SAW propagation direction (θ, middle panels) and degree of linear polarization (DOLP, upper panels) estimated for various h-BN defects (a) showing SAW-induced line splitting or (b) without an observed SAW-mediated effect. Error bars for ΔE and θ are negligible. (c) Values of θ (lower panel) and DOLP (upper panel) represented as a function of ΔE, taken from (a).

Supplementary Note 7: Density functional theory simulation of strain-induced tuning of h-BN defect state emission energy

Numerical modelling: We have studied the strain-induced changes of the optical emission energy from the anti-site nitrogen vacancy (N_BV_N) defect in a h-BN sheet illustrated in Supplementary Figure 8(a) through first-principles calculations based on spin-polarized density function theory. Our calculations are performed using the generalized gradient approximation of Perdew, Burke and Ernzerhof (GGA-PBE) [R10] for the exchange-correlation functional and ultra-soft potentials (We used the pseudopotentials N.pbe-d-rrkjus.UPF and B.pbe-rrkjus.UP, available from: http://www.quantum-espresso.org) generated with the Rappe-Rabe-Kaxiras-Joannopoulos approach [R11] to describe the electron-ion interaction as implemented in the Quantum Espresso package [R12]. The atomic positions were relaxed with a threshold of 0.005 eV/Å while electronic energy tolerance is 10^{-6} eV. The energy cut-off for the plane wave basis set is put at 50 Ry with a charge density cut-off of 400 Ry. We used a Monkhorst-Pack [R13] scheme with a $5 \times 5 \times 1$ k-mesh for the Brillouin zone integration. The calculations are based on a (6×6) supercell, with 72 atoms per h-BN layer, and a vacuum region of 15 Å between successive periodic images along the z direction. The vacancies were created by removing one nitrogen atom in the h-BN sheet. The N_BV_N defect has a nitrogen atom at a boron site neighboring a vacancy (Supplementary Figure 8(a)). No passivation by hydrogen or any other species was used in the present calculations. Our calculations take into account two relevant strain directions, the zig-zag and the arm-chair, designated in Supplementary Figure 8(a).

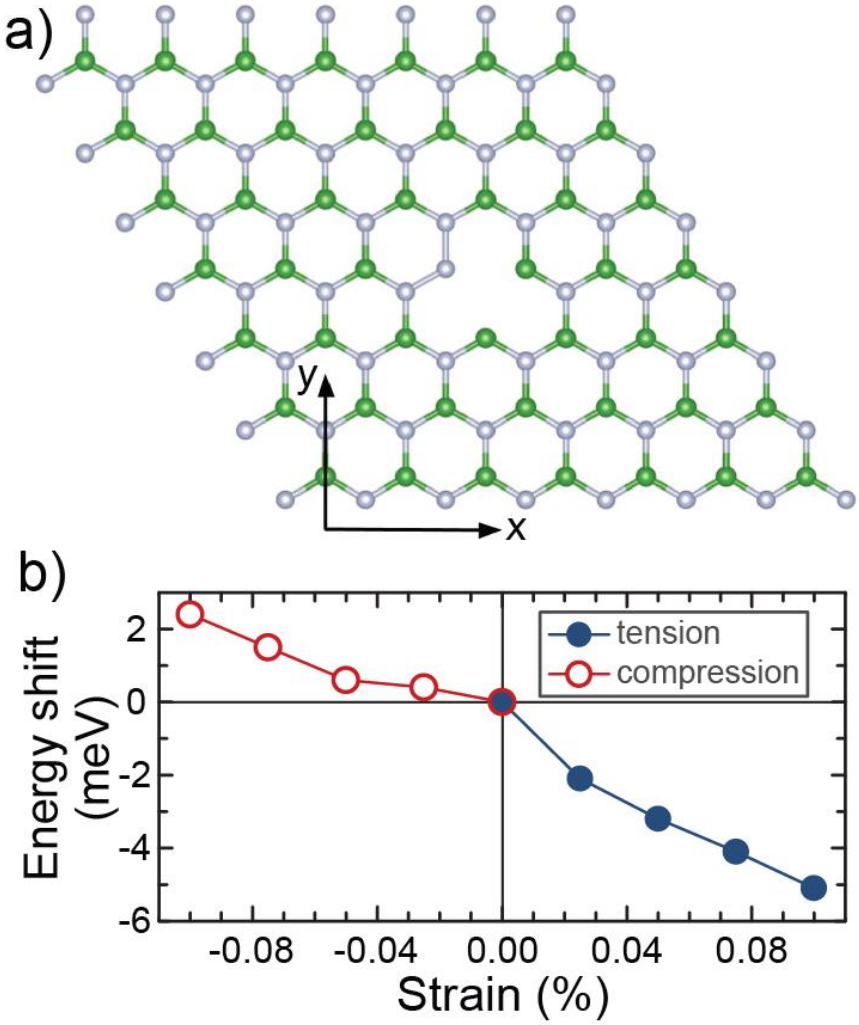

Supplementary Figure 8. (a) The relaxed atomic structure of the h-BN sheet with a N_BV_N defect, where grey and green spheres represent the nitrogen and boron atoms, respectively. The arrow lines labeled x and y indicate the zigzag and armchair material direction, respectively. (b) Calculated value of the energy shift of the N_BV_N defect emission in an h-BN sheet under externally applied uniaxial tensile (blue symbols) and compressive (red) strain along the x-direction designated in (a).

The energy shift ΔE of the optical transitions associated with the N_BV_N defect calculated for different values of both uniaxial and biaxial strain is given in Supplementary Table 1 (for tensile strain) and Supplementary Table 2 (for compressive strain). In Supplementary Figure 8(b) the calculated ΔE values are represented as a function the uniaxial strain applied along the zig-zag crystal direction (i.e. x-direction). The estimated change of the optical transition energy induced by a small uniaxial deformation (within the strain range used in our experiments) is consistent with our experimental analysis. This comparison is only qualitative, considering that the actual strain amplitude at the emitter can be smaller than the values expected on the surface of a SAW-chip. We note that the calculated energy shift is more pronounced for tensile than for compressive strain. The small asymmetry between the two strain contributions is also seen experimentally in some of the probed h-BN emitters.

Supplementary Table 1. Spin-resolved calculation of the dependence of the energy levels, energy transition (in red) and ΔE (in blue) on the tensile strain along x (zigzag), y (armchair) and $x-y$ direction (varying from 0.025% to 0.10% in steps of 0.025%) for the N_BV_N defect.

x-direction											
UP	0	0.025%	0.050%	0.075%	0.10%	**Down**	0	0.025%	0.050%	0.075%	0.10%
	-3.0014	-3.0021	-3.0051	-3.0081	-3.0111		-2.8034	-2.8085	-2.8115	-2.8145	-2.8176
	-1.5617	-1.5580	-1.5591	-1.5603	-1.5614		-0.6589	-0.6707	-0.6717	-0.6728	-0.6739
	0.2689	0.2705	0.2683	0.2662	0.2641		0.5112	0.5054	0.5034	0.5013	0.4992
transition (eV)	1.8306	1.8285	1.8274	1.8265	1.8255		2.1445	2.1378	2.1398	2.1417	2.1437
ΔE (meV)	0.0	-2.1	-3.2	-4.1	-5.1		0.0	-6.7	-4.7	-2.8	-1.0
y-direction											
UP	0	0.025%	0.050%	0.075%	0.10%	**Down**	0	0.025%	0.050%	0.075%	0.10%
	-3.0014	-3.0011	-3.0026	-3.0041	-3.0054		-2.8034	-2.8074	-2.8089	-2.8105	-2.8117
	-1.5617	-1.5592	-1.5606	-1.5625	-1.5642		-0.6589	-0.6714	-0.6726	-0.6741	-0.6753
	0.2689	0.2710	0.2697	0.2684	0.2672		0.5112	0.5057	0.5044	0.5029	0.5017
transition (eV)	1.8306	1.8302	1.8303	1.8309	1.8314		2.1445	2.1360	2.1363	2.1364	2.1364
ΔE (meV)	0.0	-0.4	-0.3	-0.3	-1.0		0.0	-8.5	-8.2	-8.1	-8.1
xy-direction (bi-axial)											
UP	0	0.025%	0.050%	0.075%	0.10%	**Down**	0	0.025%	0.050%	0.075%	0.10%
	-3.0014	-3.0028	-3.0073	-3.0118	-3.0161		-2.8034	-2.8092	-2.8137	-2.8183	-2.8225
	-1.5617	-1.5599	-1.5624	-1.5655	-1.5683		-0.6589	-0.6720	-0.6742	-0.6768	-0.6792
	0.2689	0.2697	0.2664	0.2629	0.2596		0.5112	0.5045	0.5011	0.4976	0.4943
transition (eV)	1.8306	1.8296	1.8288	1.8284	1.8279		2.1445	2.1372	2.1395	2.1415	2.1433
ΔE (meV)	0.0	-1.0	-1.8	-2.2	-2.7		0.0	-7.3	-5.0	-3.0	-1.2

Supplementary Table 2. Spin-resolved calculation of the dependence of the energy levels, energy transition (in red) and ΔE (in blue) on the compressive strain along x (zigzag), y (armchair) and $x-y$ direction (varying from 0.025% to 0.10% in steps of 0.025%) for the N_BV_N defect.

x-direction											
UP	0	0.025%	0.050%	0.075%	0.10%	**Down**	0	0.025%	0.050%	0.075%	0.10%
	-3.0014	-2.9969	-2.9941	-2.9913	-2.9884		-2.8034	-2.8033	-2.8004	-2.7976	-2.7947
	-1.5617	-1.5560	-1.5549	-1.5538	-1.5527		-0.6589	-0.6688	-0.6677	-0.6667	-0.6657
	0.2689	0.2742	0.2763	0.2783	0.2803		0.5112	0.5090	0.5110	0.5130	0.5149
transition (eV)	1.8306	1.8302	1.8312	1.8321	1.8330		2.1445	2.1345	2.1327	2.1309	2.1290

ΔE (meV)	0.0	0.4	0.6	1.5	2.4		0.0	10.0	11.8	13.6	15.5
y-direction											
UP	0	0.025%	0.050%	0.075%	0.10%	**Down**	0	0.025%	0.050%	0.075%	0.10%
	-3.0014	-2.9983	-2.9969	-2.9955	-2.9940		-2.8034	-2.8047	-2.8033	-2.8019	-2.8005
	-1.5617	-1.5553	-1.5535	-1.5517	-1.5499		-0.6589	-0.6684	-0.6670	-0.6656	-0.6642
	0.2689	0.2734	0.2747	0.2759	0.2772		0.5112	0.5084	0.5098	0.5111	0.5125
transition (eV)	1.8306	1.8287	1.8282	1.8276	1.8271		2.1445	2.1363	2.1363	2.1363	2.1363
ΔE (meV)	0.0	1.9	2.4	3.0	3.5		0.0	8.2	8.2	8.2	8.2
xy-direction (bi-axial)											
UP	0	0.025%	0.050%	0.075%	0.10%	**Down**	0	0.025%	0.050%	0.075%	0.10%
	-3.0014	-2.9954	-2.9926	-2.9869	-2.9827		-2.8034	-2.8018	-2.7990	-2.7933	-2.7890
	-1.5617	-1.5542	-1.5506	-1.5484	-1.5456		-0.6589	-0.6673	-0.6645	-0.6624	-0.6600
	0.2689	0.2755	0.2780	0.2821	0.2853		0.5112	0.5105	0.5132	0.5171	0.5204
transition (eV)	1.8306	1.8231	1.8286	1.8305	1.8309		2.1445	2.1420	2.1345	2.1288	2.1290
ΔE (meV)	0.0	7.5	2.0	0.1	0.3		0.0	2.5	10.0	15.7	15.5

Supplementary References

[R1] Horcas, I. & Fernández, R. WSXM: A software for scanning probe microscopy and a tool for nanotechnology. *Rev. Sci. Instrum.* **78**, 013705 (2007).

[R2] Gimeno, A. *et al.* 'Flatten plus': a recent implementation in WSxM for biological research. *Bioinformatics* **31**, 2918-2920 (2015).

[R3] Nemes-Incze, P., Osváth, Z., Kamarás, K. & Biró, L. P. Anomalies in thickness measurements of graphene and few layer graphite crystals by tapping mode atomic force microscopy. *Carbon* **46**, 1435-1442 (2008).

[R4] Tran, T. T. *et al.* Robust multicolor single photon emission from point defects in hexagonal boron nitride. *ACS Nano* **10**, 7331-7338 (2016).

[R5] Jungwirth, N. R. & Fuchs, G. D. Optical absorption and emission mechanisms of single defects in hexagonal boron nitride. *Phys. Rev. Lett.* **119**, 057401 (2017).

[R6] Brouri, R., Beveratos, A., Poizat, J. –P. & Grangier, P. Photon antibunching in the fluorescence of individual color centers in diamond. *Opt. Lett.* **25**, 1294-1296 (2000).

[R7] Beveratos, A. *et al.* Room temperature stable single-photon source. *Eur. Phys. J. D* **18**, 191-196 (2002).

[R8] Kitson, S. C., Jonsson, P., Rarity, J. G. & Tapster, P. R. Intensity fluctuation spectroscopy of small numbers of dye molecules in a microcavity. *Phys. Rev. A* **58**, 620 (1998).

[R9] de Lima Jr., M. M. & Santos, P. V. Modulation of photonic structures by surface acoustic waves. *Rep. Prog. Phys.* **68**, 1639-1701 (2005).

[R10] Perdew, J. P., Burke, K. & Ernzerhof M. Generalized gradient approximation made simple. *Phys. Rev. Lett.* **77**, 3865-3868 (1996).

[R11] Rappe, A. M., Rabe, K. M., Kaxiras, E. & Joannopoulos, J. D. Optimized pseudopotentials. *Phys. Rev. B* **41**, 1227-1230 (1990).

[R12] Giannozzi, P., et al. Quantum espresso: A modular and open-source software project for quantum simulations of materials. *J. Phys.: Condens. Matter* **21**, 395502 (2009).
[R13] Monkhorst, H. J. & Pack, J. D. Special points for Brillouin-zone integrations. *Phys. Rev. B* **13**, 5188-5192 (1976).